

Synthesized multiwall MoS₂ nanotube and nanoribbon field-effect transistors

S. Fathipour,^{1,a)} M. Remskar,² A. Varlec,² A. Ajoy,¹ R. Yan,³ S. Vishwanath,¹ S. Rouvimov,¹ W. S. Hwang,⁴ H. G. Xing,¹ D. Jena,¹ and A. Seabaugh^{1,b)}

¹Department of Electrical Engineering, University of Notre Dame, Notre Dame, Indiana 46556, USA

²Solid State Physics Department, Jožef Stefan Institute, Ljubljana, Slovenia

³Department of Electrical Engineering, Cornell University, Ithaca, New York 14850, USA

⁴Department of Materials Engineering, Korea Aerospace University, Gyeonggi 412791, Korea

(Received 20 November 2014; accepted 5 January 2015; published online 16 January 2015)

We report on the fabrication and characterization of synthesized multiwall MoS₂ nanotube (NT) and nanoribbon (NR) field-effect transistors (FETs). The MoS₂ NTs and NRs were grown by chemical transport, using iodine as a transport agent. Raman spectroscopy confirms the material as unambiguously MoS₂ in NT, NR, and flake forms. Transmission electron microscopy was used to observe cross sections of the devices after electrical measurements and these were used in the interpretation of the electrical measurements, allowing the estimation of the current density. The NT and NR FETs demonstrate *n*-type behavior, with ON/OFF current ratios exceeding 10³, and with current densities of 1.02 μA/μm and 0.79 μA/μm at V_{DS}=0.3 V and V_{BG}=1 V, respectively. Photocurrent measurements conducted on a MoS₂ NT FET revealed short-circuit photocurrent of tens of nanoamps under an excitation optical power of 78 μW and 488 nm wavelength, which corresponds to a responsivity of 460 μA/W. A long channel transistor model was used to model the common-source characteristics of MoS₂ NT and NR FETs and was shown to be consistent with the measured data. © 2015 AIP Publishing LLC. [<http://dx.doi.org/10.1063/1.4906066>]

There is a growing interest in atom-thick materials such as graphene and the transition metal dichalcogenides (TMDs) for electronics applications.^{1,2} Bulk and single layer sheets of TMDs are beginning to be explored in a wide range of optoelectronic and electronic devices including solar cells,^{3,4} photodetectors,^{5,6} sensors,^{7,8} field-effect transistors (FETs),^{9–12} and logic circuits.^{13,14} The absence of surface dangling bonds, the excellent gate electrostatics of the few-layer transistor, and the potential for large area planar processing are all motivating this research. While planar processing is desirable for manufacturing, at the limits of scaling, the properties of these materials may be compromised by unpassivated dangling bonds at the sheet edges. Edges introduce traps, which can degrade subthreshold swing and increase tunneling leakage, 1/*f* noise, and variability in the device characteristics. Edges can be substantially eliminated by using nanotubes (NTs) and nanoribbons (NRs) formed from collapsed NTs.

There are only a few experimental reports of TMD NT transistors and these are based on WS₂^{15,16} and MoS₂.^{17,18} Density functional theory shows that WS₂ and MoS₂ NTs are semiconducting with well-defined band gaps.^{19,20} Levi *et al.*¹⁵ reported *n*-channel conduction on a 75 nm diameter WS₂ multiwall NTs with an ON/OFF current ratio of about 2; this commercial material was dispersed from powder. Unalan *et al.*¹⁶ used multiwall NTs synthesized by conversion of tungsten oxide particles;²¹ the ON/OFF current ratio was about 4. The first MoS₂ NT FET report by Remskar *et al.*¹⁷ showed no gate modulation and no photoresponse on a multiwall NT with a diameter of approximately 100 nm and synthesized from Mo₆S₄I₆ nanowires by sulphurization

using H₂S/H₂/Ar gas mixture, the method that causes a high density of structural defects.²² In a recent report, Strojnik *et al.*¹⁸ confirmed transistor action with *n*-channel conduction in MoS₂ NTs based on the same synthesis method and achieved an ON/OFF current ratio of 60. In this paper, we report on the properties of MoS₂ NT and NR FETs in which an ON/OFF current ratio exceeding 10³ is achieved.

The NTs used in this study were grown by chemical transport reaction, which enables growth of NTs with very slow rate from the vapor phase.²³ The silica ampoule containing MoS₂ powder and iodine in amount of 1.5 mg/cm³ was evacuated and sealed at a pressure of 7 × 10⁻⁴ Pa. The transport reaction using iodine as a transport agent ran from 1133 K to 1010 K with a temperature gradient of 6.2 K/cm in a two-zone furnace. After 3 weeks of growth, the silica ampoules were cooled to room temperature with a controlled cooling rate of 60 °C/h. Approximately, a few percent of the starting material was transported by the reaction to form nanotubes, while the rest of the transported material grows as strongly undulated thin plate-like crystals. The nearly equilibrium growth conditions enable the synthesis of nanotubes of different diameters, length, and wall thickness, but with extremely low density of structural defects. They grow up to several millimeters in length. The diameters in multiwall nanotubes range from several micrometers to less than ten nanometers. Some of the nanotubes spontaneously collapse during the growth and continue the growth in ribbon shapes.²⁴

The completed transistor planar views and schematic cross section are shown in Figure 1. The process flow consisted of electron-beam evaporation of Ti/Au (5/100 nm) on the back of the Si wafer. The MoS₂ nanostructures were exfoliated using 3M Scotch 810 tape onto 26 nm Al₂O₃ formed by atomic layer deposition. The NTs and NRs were

^{a)}Electronic mail: sfathipo@nd.edu

^{b)}Electronic mail: seabaugh.1@nd.edu

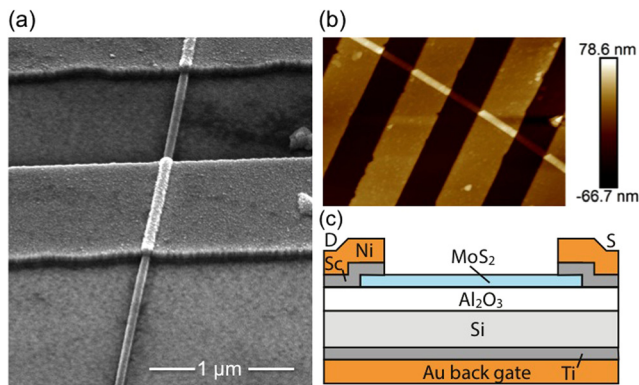


FIG. 1. (a) SEM image, (b) AFM image, and (c) schematic cross-section of a MoS₂ NT FET. The four-contacts Kelvin connection shown in (b) was used to measure the contact resistance.

then patterned to form the source and drain contacts using electron beam lithography followed by deposition of Sc/Ni (40 nm/20 nm) metal contacts. Figure 1 shows (a) scanning electron microscope (SEM) image, (b) atomic force microscope (AFM) image, and (c) schematic cross section of the FET.

Transmission electron microscope (TEM) images were taken following the electrical measurements to establish clearly the cross section of the measured devices. Figs. 2(a) and 2(b) are of the NR and Fig. 2(c) shows the NT. Both nanostructures are multiwall and the ribbon is a collapsed nanotube with a total thickness of about 7 nm and 10 monolayers. This would give an interlayer distance of 0.7 nm for the NR. As shown by the TEM image of Fig. 2(c), NT has an elliptical shape with a wall thickness of 11 layers. Interlayer distance in NT based on the TEM results is 0.68 nm. The interlayer distance in both NR and NT is close to the range of 0.62–0.68, as reported in literature.^{25–27}

Raman measurements, shown in Fig. 3(a), were performed on the NR, the NT, and a flake that was exfoliated from the same material source. Measurements were done in the backscattering configuration using a WITec Alpha 300 system at room temperature (100× objective, 488 nm laser wavelength, and 494 μW power). Clear signals of Raman in-plane vibrational mode, E_{2g}^1 , and out-of-plane vibrational mode, A_{1g} , for MoS₂ are observed in all the grown nanostructures. A red shift is observed in the Raman peaks of the NT and NR structures relative to the flake. Local heating due to laser illumination is known to red shift both the E_{2g}^1 and A_{1g} peaks in bulk and few-layered MoS₂ as well as in MoS₂ microtubes.^{28,29} Measurements of the power dependence of the Raman peaks, shown in the supplementary material,³⁰ clearly show the NT Raman spectra shift with laser power. The conduction of heat out of the NT may be expected to be less than the NR because of smaller contact area to the substrate. Thus, heat may be expected to red shift the NT more than the NR.

A smaller E_{2g}^1 over A_{1g} ratio was observed in the NT. This could be explained by the fact that in the back-scattering configuration, polarization of incoming light is perpendicular to the *c*-axis of the crystal in the NR, bulk MoS₂ and center of NT, while it is parallel to the *c*-axis at the edges of the NT. Direction of the A_{1g} mode vibration is parallel to the *c*-axis³¹

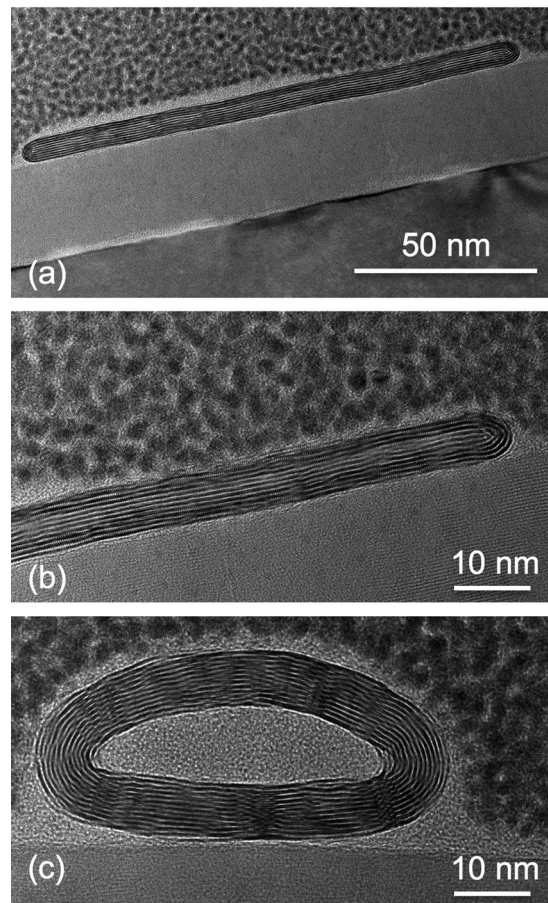


FIG. 2. Transmission electron microscope image of the transistor channel cross sections: (a) MoS₂ nanoribbon with width of 140 nm, height of 7 nm, and cross sectional area of 980 nm². The nanoribbon has a layer thickness of 10 monolayers. (b) MoS₂ nanoribbon magnified to show wrapping of the layers at the ribbon edge. (c) MoS₂ NT with a layer thickness of 11 monolayers and cross sectional area of 766 nm². The minor and major radii for the inner ellipse are 5 nm and 20 nm, respectively, and for the outer ellipse are 12.5 nm and 27.5 nm.

and therefore its intensity increases at nanotube edges. The edges can contribute majority of the signal when diameter of NT is as small as tens of nanometers.

The measured drain current per unit width vs. back-gate voltage is shown in Fig. 3(b) for a NT and two NR FETs, designated NR1 and NR2. All transistors showed *n*-channel conduction, with ON/OFF current ratios of more than 10³. In the course of the measurement, the reverse bias was limited to −1.5 V, wherein the leakage current was less than a few pA. As a result, the value of 10³ for the NT and NR2 FET should be considered as a lower limit. This value for the NT FET far exceeds the prior best report of 60 by Strojnik *et al.*,¹⁸ presumably due to defects and structure related to the different methods of synthesis. The MoS₂ NTs of Strojnik's report were formed using a two-step synthesis method involving the formation of MoSI nanowires followed by conversion in an Ar/H₂S/H₂ ambient to MoS₂ NTs, while the NTs discussed here utilized a direct synthesis by chemical transport using iodine.

From the measured dimensions given in the caption of Fig. 2, the width for the NT and the NR1 can be estimated to be 55 nm and 140 nm. The measured width for NR2 is 321 nm. The corresponding values for the extracted current

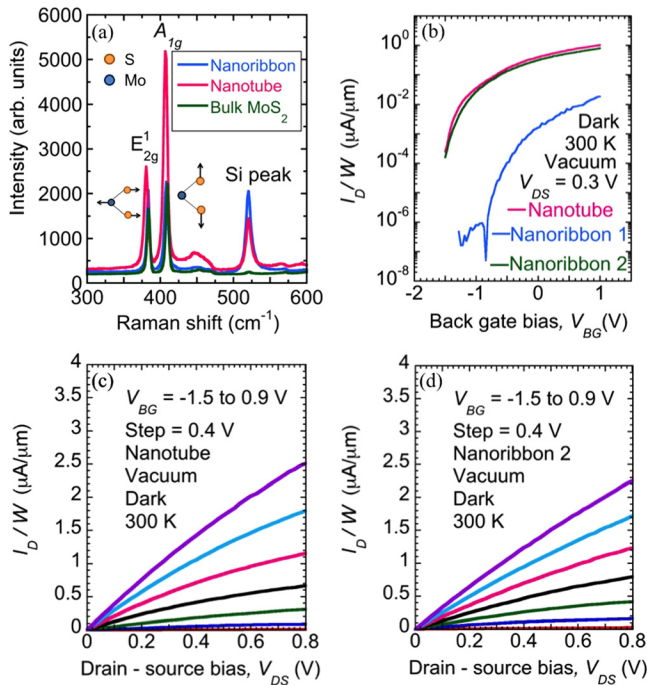


FIG. 3. (a) Raman spectrum of the MoS₂ NT, NR, and bulk MoS₂ flake with a laser wavelength of 488 nm and power of 494 μ W. The out-of-plane A_{1g} and in-plane E_{2g}¹ vibrations are identified in the inset. (b) Measured drain current per unit width vs. back-gate voltage for the MoS₂ NT FET and two MoS₂ NR FETs, designated NR1 and NR2. Channel widths are 55 nm, 140 nm, and 321 nm, respectively. (c) Common source characteristics for the MoS₂ NT FET measured in vacuum. (d) Common source characteristics for the MoS₂ NR2 FET measured in vacuum.

per unit width measured in NT, NR1, and NR2 FETs are 1.02 μ A/ μ m, 0.02 μ A/ μ m, and 0.79 μ A/ μ m at $V_{DS} = 0.3$ V and $V_{BG} = 1$ V. The lower current density in NR1 FET is not well explained by contacts or mobility and remains a question.

The electrical characteristics of the back-gated MoS₂ NT and NR2 FETs are further modeled using a long channel FET model. The detailed description of this model is included in the supplementary material.³⁰ Carrier density, mobility, and flat band voltage are the unknowns in the model. Using a nominal charge density of 1×10^{16} cm⁻³, mobility of 43.5 cm²/V s, and flat band voltage of -0.9 V for the MoS₂ NT FET and a charge density of 1×10^{16} cm⁻³, mobility of 36 cm²/V s and flat band voltage of -1 V for the MoS₂ NR2 FET, an excellent fit to the experimental data was obtained. Of these parameters, mobility ($\sim \pm 6.4\%$) and flat band voltage ($\sim \pm 10\%$) can be determined within a fairly narrow range. On the other hand, the doping density can vary up to an order of magnitude. See supplementary material³⁰ for details.

The sole report of MoS₂ NR FETs, by Liu *et al.*,³² utilized reactive ion etching to form ribbons as narrow as 60 nm from exfoliated flakes. Liu *et al.* achieved an ON/OFF current ratio of nearly 10^4 on n-channel FETs for a 60 nm NR width with a 6 nm thickness. This exceeds the 10^3 ON/OFF ratio obtained here. Subthreshold swing is much improved in this paper. Our minimum subthreshold swing for both NR FETs is 200 mV/decade, compared to 10 V/decade in the MoS₂ NR FET by Liu *et al.*³² The enhanced subthreshold swings in the NR can be attributed to two factors. First, the

NR in our FET is grown. Therefore, edge roughness and defects due to dangling bonds are largely nonexistent. This is in contrast with the NRs formed by plasma dry etching of MoS₂ flakes by Liu *et al.* Second, to fabricate devices, we use 26 nm of Al₂O₃, whereas Liu *et al.* use 300 nm SiO₂. This will extend the SS by factor of 10 \times , bringing the two results more closely in line.

Four point probe measurements were used to extract the contact resistance of the MoS₂ NT FET with a Sc contact. The extracted value for contact resistance at $V_{BG} = 0$ V was 39.6 k Ω μ m. This exceeds the reported value of 10 k Ω μ m by Das and Appenzeller in Ref. 33 for same overdrive voltage and with same contact on MoS₂. As outlined by Das and Appenzeller,³³ the extracted resistance involves contributions from both Schottky barrier resistance and also resistive coupling between the layers of the 2D material. Therefore, the resistance due to the Schottky barriers may be less than this value.

Scanning photocurrent measurements were conducted on MoS₂ NT FETs, prepared from the same synthesis batch. These FETs utilized Ti/Au (1 nm/100 nm) source and drain contacts on a highly doped Si wafer covered by 285 nm SiO₂. The strong photoresponse of these Schottky barrier contacts motivated a change in metallization to Sc to provide a lower electron Schottky barrier. A WITec Alpha 300 scanning confocal microscope was used to focus a 488 nm wavelength laser onto the NT FET. The diffraction-limited beam diameter is estimated to be $1.22\lambda/\text{NA} = 0.66$ μ m, where λ is the excitation wavelength, and NA is the numerical aperture (0.9 for a 100 \times objective lens). Using spot area and the measured laser power, a power density of 22 kW/cm² was determined. Photocurrent was recorded as the laser spatially scanned the sample. Current was converted to a voltage using a transimpedance amplifier. The reflected light was simultaneously collected to correlate with the spatial photocurrent mapping. Fig. 4(a) shows a representative short-circuit photocurrent ($V_{DS} = V_{BG} = 0$) mapping of a MoS₂ NT FET, with the metal 1 as drain, metal 2 as floating, and metal 3 as source. Fig. 4(b) shows the photocurrent profile along the blue dotted line of Fig. 4(a). Prominent negative and positive photocurrents are detected at the drain and source side,

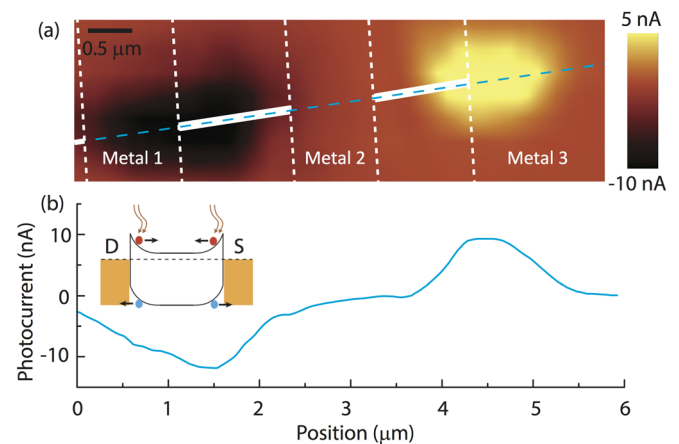


FIG. 4. (a) Representative short-circuit photocurrent mapping of a MoS₂ NT FET. (b) The line profile is the photocurrent along the dotted blue line in (a). The inset shows the schematic of the band bending in the MoS₂ NT device. Blue and red carriers refer to holes and electrons, respectively.

respectively. The photocurrent is due to the separation of photogenerated carriers by band bending at the metal-semiconductor junctions, which dominate the voltage drop in the TMD FET. Responsivity is defined as the ratio of photocurrent, divided by the incident power on the nanotube. The incident power on the nanotube was found by multiplying the total power of the laser and the area ratio of the nanotube and laser spot. These measurements, which we use to characterize the zero-bias band bending, indicate a short-circuit responsivity of $\sim 460 \mu\text{A/W}$. There are reports of higher responsivity under bias.^{34–39}

Using the Schottky photocurrent mapping of Fig. 4(b), we estimate the band bending profile near source/MoS₂ junction and drain/MoS₂ junction. When the NT is illuminated near the drain or source contact, electron/hole pairs are locally generated at the illumination region. Under the built-in Schottky field at NT/metal junction, the electron and the hole are separated with the current direction set by the band bending. To match the observed photocurrent polarity, the bands are bent upward, as indicated in the band diagram shown in the inset of Fig. 4(b).

In conclusion, synthesized MoS₂ NT and NR FETs were fabricated and characterized. Devices demonstrated *n*-type characteristics with ON/OFF current ratios of more than 10³, greatly exceeding the best prior report of 60 in the NT case. Raman measurements confirm the E_{2g}¹ and A_{1g} vibrational modes in both tubes and ribbons with a red shift compared to bulk MoS₂, due to laser heating effect. Photocurrent measurements were conducted on MoS₂ NT FET with Ti/Au contacts and revealed a responsivity of $\sim 460 \mu\text{A/W}$. The common-source characteristics were shown to be in good agreement with a long channel transistor model.

This work was supported in part by the Center for Low Energy Systems Technology (LEAST), a STARnet Semiconductor Research Corporation program sponsored by MARCO and DARPA.

¹D. Jena, *Proc. IEEE* **101**, 1585 (2013).

²G. Fiori, F. Bonaccorso, G. Iannaccone, T. Palacios, D. Neumaier, A. Seabaugh, S. K. Banerjee, and L. Colombo, *Nat. Nanotechnol.* **9**, 768 (2014).

³M. L. Tsai, S. H. Su, J. K. Chang, D. S. Tsai, C. H. Chen, C. I. Wu, L. J. Li, L. J. Chen, and J. H. He, *ACS Nano* **8**, 8317 (2014).

⁴G. Prasad and O. N. Srivastava, *J. Phys. D: Appl. Phys.* **21**, 1028 (1988).

⁵N. Huo, S. Yang, Z. Wei, S. S. Li, J. B. Xia, and J. Li, *Sci. Rep.* **4**, 5209 (2014).

⁶B. Baugher, H. Churchill, Y. Yang, and P. Herrero, *Nat. Nanotechnol.* **9**, 262 (2014).

⁷D. J. Late, Y. K. Huang, B. Liu, J. Acharya, S. N. Shirodkar, J. Luo, A. Yan, D. Charles, U. V. Waghmare, V. P. Dravid, and C. N. R. Rao, *ACS Nano* **7**, 4879 (2013).

⁸F. K. Perkins, A. L. Friedman, E. Cobas, P. M. Campbell, G. G. Jernigan, and B. T. Jonker, *Nano Lett.* **13**, 668 (2013).

⁹B. Radisavljevic, A. Radenovic, J. Brivio, V. Giacometti, and A. Kis, *Nat. Nanotechnol.* **6**, 147 (2011).

¹⁰S. Fathipour, W. S. Hwang, T. H. Kosel, H. Xing, W. Haensch, D. Jena, and A. C. Seabaugh, in *Device Research Conference (DRC)*, pp. 115–116.

¹¹S. Fathipour, N. Ma, W. S. Hwang, V. Protasenko, S. Vishwanath, H. G. Xing, H. Xu, D. Jena, J. Appenzeller, and A. Seabaugh, *Appl. Phys. Lett.* **105**, 192101 (2014).

¹²W. S. Hwang, M. Remskar, and R. Yan, *Appl. Phys. Lett.* **101**, 013107 (2012).

¹³M. Tosun, S. Chuang, H. Fang, A. B. Sachid, M. Hettick, Y. Lin, Y. Zeng, and A. Javey, *ACS Nano* **8**, 4948 (2014).

¹⁴B. Radisavljevic, M. B. Whitwick, and A. Kis, *ACS Nano* **7**, 3729 (2013).

¹⁵R. Levi, O. Bitton, G. Leitner, R. Tenne, and E. Joselevich, *Nano Lett.* **13**, 3736 (2013).

¹⁶H. E. Unalan, Y. Yang, Y. Zhang, P. Hiralal, D. Kuo, S. Dalal, T. Butler, S. N. Cha, J. E. Jang, K. Chremmou, G. Lentaris, D. Wei, R. Rosentsveig, K. Suzuki, H. Matsumoto, M. Minagawa, Y. Hayashi, M. Chhowalla, A. Tanioka, W. I. Milne, R. Tenne, and G. A. J. Amaratunga, *IEEE Trans. Electron Devices* **55**, 2988 (2008).

¹⁷M. Remskar, A. Mrzel, M. Virsek, M. Godec, M. Krause, A. Kolitsch, A. Singh, and A. Seabaugh, *Nanoscale Res. Lett.* **6**, 26 (2011).

¹⁸M. Strojnik, A. Kovic, A. Mrzel, J. Buh, J. Strle, and D. Mihailovic, *AIP Adv.* **4**, 097114 (2014).

¹⁹G. Seifert, H. Terrones, M. Terrones, G. Jungnickel, and T. Frauenheim, *Phys. Rev. Lett.* **85**, 146 (2000).

²⁰G. Seifert, H. Terrones, M. Terrones, G. Jungnickel, and T. Frauenheim, *Solid State Commun.* **114**, 245 (2000).

²¹A. Rothschild, J. Sloan, and R. Tenne, *J. Am. Chem. Soc.* **122**, 5169 (2000).

²²M. Virsek, N. Novak, C. Filipic, P. Kump, M. Remskar, and Z. Kutnjak, *J. Appl. Phys.* **112**, 103710 (2012).

²³M. Remskar, Z. Skraba, M. Regula, C. Ballif, R. Sanjines, and F. Levy, *Adv. Mater.* **10**, 246 (1998).

²⁴M. Remskar, Z. Skraba, F. Cleton, R. Sanjines, and F. Levy, *Surf. Rev. Lett.* **5**, 423 (1998).

²⁵X. Zhang, W. P. Han, J. B. Wu, S. Milana, Y. Lu, Q. Q. Li, A. C. Ferrari, and P. H. Tan, *Phys. Rev. B* **87**, 115413 (2013).

²⁶Y. Zhan, Z. Liu, S. Najmaei, P. M. Ajayan, and J. Lou, *Small* **8**, 966 (2012).

²⁷P. D. Fleischauer, R. Jeffrey, P. Lince, A. Bertrand, and R. Bauer, *Langmuir* **5**, 1009 (1989).

²⁸M. Virsek, M. Krause, A. Kolitsch, and M. Remskar, *Phys. Status Solidi B* **246**, 2782 (2009).

²⁹S. Najmaei, Z. Liu, P. M. Ajayan, and J. Lou, *Appl. Phys. Lett.* **100**, 013106 (2012).

³⁰See supplementary material at <http://dx.doi.org/10.1063/1.4906066> for more details on the analytical model and power dependence of Raman peaks.

³¹T. J. Wieting and J. L. Verble, *Phys. Rev. B* **3**, 4286 (1971).

³²H. Liu, J. Gu, and P. Ye, *IEEE Electron Device Lett.* **33**, 1273 (2012).

³³S. Das and J. Appenzeller, *Nano Lett.* **13**, 3396 (2013).

³⁴O. Lopez-Sanchez, D. Lembke, M. Kayci, A. Radenovic, and A. Kis, *Nat. Nanotechnol.* **8**, 497 (2013).

³⁵W. Choi, M. Y. Cho, A. Konar, J. H. Lee, G. B. Cha, S. C. Hong, S. Kim, J. Kim, D. Jena, J. Joo, and S. Kim, *Adv. Mater.* **24**, 5832 (2012).

³⁶Z. Yin, H. Li, H. Li, L. Jiang, Y. Shi, Y. Sun, G. Lu, Q. Zhang, X. Chen, and H. Zhang, *ACS Nano* **6**, 74 (2012).

³⁷Y. Li, C. Y. Xu, J. Y. Wang, and L. Zhen, *Sci. Rep.* **4**, 7186 (2014).

³⁸M. R. Esmaeili-Rad and S. Salahuddin, *Sci. Rep.* **3**, 2345 (2013).

³⁹W. Zhang, C. P. Chuu, J. K. Huang, C. H. Chen, M. L. Tsai, Y. H. Chang, C. T. Liang, Y. Z. Chen, Y. L. Chueh, J. H. He, M. Y. Chou, and L. J. Li, *Sci. Rep.* **4**, 3826 (2014).